Antimony substituted lanthanum orthoniobate proton conductor – structure and electronic properties.

Aleksandra Mielewczyk-Gryń*[1], Sebastian Wachowski[1], Agnieszka Witkowska[1], Kacper Dzierzgowski[1], Wojciech Skubida[1,2], Konrad Świerczek[2], Anna Regoutz[3,4], David J. Payne[4], Stephen Hull[5], Hangfeng Zhang[6], Isaac Abrahams[6] and Maria Gazda[1]

[1] Department of Solid State Physics, Faculty of Applied Physics and Mathematics, and Advanced Materials Center, Gdańsk University of Technology Narutowicza 11/12 80-233 Gdańsk, Poland

[2]Faculty of Energy and Fuels, AGH University of Science and Technology Mickiewicza 30, 30-059, Krakow, Poland

[3]Department of Chemistry, University College London, Gower St, Bloomsbury, London WC1E 6BT, UK

[4]Department of Materials, Imperial College London, Exhibition Road, London, SW7 2AZ, UK

[5]STFC ISIS Facility, Rutherford Appleton Laboratory, Chilton, Didcot, Oxon OX11 0QX, UK

[6]Materials Research Institute, School of Biological and Chemical Sciences Queen Mary University of London, Mile End Road London E1 4NS, UK

Corresponding Author

*e-mail: alegryn@pg.edu.pl, +48 58 348 66 19

ORCID

Aleksandra Mielewczyk-Gryń 0000-0001-6795-3840, Sebastian Wachowski 0000-0003-3752-0432, Agnieszka Witkowska 0000-0002-1878-8049, Kacper Dzierzgowski 0000-0002-1413-7767, Wojciech Skubida 0000-0003-3036-4975, Konrad Świerczek 0000-0003-4519-389X, Anna Regoutz 0000-0002-3747-3763, David J. Payne 0000-0002-2120-6679, Stephen Hull 0000-0001-6078-3463, Hangfeng Zhang 0000-0002-3928-8772, Isaac Abrahams 0000-0002-8606-6056, and Maria Gazda 0000-0001-6193-7815

Keywords: Fuel cell materials, Neutron diffraction, Extended X-ray absorption fine structure, Superionic conductor, Phase transition

Abstract

X-ray and neutron diffraction have been utilized to analyze the crystalline and electronic structure of lanthanum orthoniobate substituted by antimony. Using X-ray absorption spectroscopy and photoelectron spectroscopy, changes in the electronic structure of the material upon substitution have been analyzed. The structural transition temperature between fergusonite and scheelite phases for 30 mol% antimony substitution was found to be 15 °C. Based on the neutron data, the oxygen nonstoichiometry was found to be relatively low. Moreover, no influence on the position of the valence band maximum was observed. The influence of the protonation on the electronic structure of constituent oxides has been studied. Absorption data show that the incorporation of protonic defects into the lanthanum orthoniobate structure leads to changes in lanthanum electronic structure and to a decrease in the density of unoccupied electronic states.

1. Introduction

Systems based on lanthanum orthoniobate have been widely investigated for more than a decade as promising proton conducting materials for electrochemical devices. Since protons are not native to the lattice of lanthanum orthoniobates, proton conduction in these materials requires the incorporation of protons as positively charged hydroxide defects (protonic defects), which occur primarily via the hydration reaction (1).

$$H_2O + V_O^{\bullet\bullet} + O_O^{\times} \rightarrow 2OH_O^{\bullet} \qquad (1)$$

The amount of protons incorporated into the structure and the protonic defect mobility are the two crucial features that influence the electrochemical performance of materials in working devices.

In recent years, considerable effort has been put into suppressing the structural phase transition between monoclinic and tetragonal structures observed in these oxides at temperatures above room temperature. For example, in $LaNbO_{4-\delta}$ the phase transition occurs at around 500 °C [1–3]. The main strategy for shifting the phase transition temperature is the substitution of niobium by other penta- or tri-valent elements like antimony [4–7], vanadium [7–9], arsenic [10], or tantalum [7, 11–13]. Differences in ionic radius and electronegativity compared to niobium result in either elevating (for Ta) or decreasing (for Sb, V, and As) the transition temperature [10].

The change in phase transition temperature, due to niobium site substitution, is accompanied by changes in properties like the thermal expansion coefficient [14, 15], and activation energy of conductivity [16]. It has been shown that both vanadium and antimony substitutions influence phonon properties [6, 9, 17]. In our recent study, we reported that both A-site (with calcium) and B-site (with antimony) substitutions in lanthanum orthoniobate increase its water uptake [18]. Moreover, the introduction of dopants elevated not only the water uptake, but also the protonic conductivity of these compounds [5]. It is expected that such modifications change not only the crystal structure, as has been previously reported [7], but also the electronic structure.

In this work, the results of X-ray and neutron diffraction and X-ray absorption and photoelectron spectroscopic studies of lanthanum orthoniobate substituted with antimony are presented and analyzed. The aim of these analyses is to provide information on how isovalent substitution on the Nb site affects local ordering and selected features of the electronic structure of the system. Here, we analyze the effect of protonic defect formation on the electronic structure in these materials, which represents one of the first studies of this type on a ceramic proton conductor. Through variable temperature X-ray diffraction measurements, the phase fergusonite ↔ scheelite transition, in 30% mol % Sb substituted lanthanum orhoniobate is shown to occur at ca. 15 °C, leaving the scheelite phase stable at room temperature. This phase has more desirable properties in terms of protonic conductivity and thermal expansion coefficient.

2. Experimental

$LaNb_{1-x}Sb_xO_4$ with x = 0.0, 0.1, 0.2, 0.25 and 0.3 were synthesized using a two-step solid-state reaction. La_2O_3 (99.99 %, Aldrich, preheated at 900 °C for 4 h), Sb_2O_3 (99.99 %, Aldrich), and Nb_2O_5 (99.99 %, Alfa Aesar) were used as starting materials. The precursors were hand milled in an agate mortar in isopropanol and then dried. The obtained powders were uniaxially pressed at 400 MPa into 12 mm diameter pellets. The green bodies were calcined at 1200 °C for 12 h and after cooling were ground into powders. Samples were then re-pelletized and sintered at 1200 °C for a further 12 h. Prior to subsequent analysis, the sintered samples were crushed and ball milled in isopropanol. The samples for spectroscopic studies were also submitted to a hydration process, reflecting the water uptake studies described in our previous work [18], where a small quantity of powder was protonated by heating in a water-rich atmosphere followed by cooling to room temperature. Two batches of samples were prepared: one dried in dry air (80 N_2/20 O_2) for 3 h, and one protonated at 300 °C in wet air (80 N_2/20 O_2) (pH_2O = 0.023 atm) for 3 h.

The phase composition of the synthesized samples was checked with powder X-ray diffraction (PXRD) using Cu-Kα radiation. Room temperature measurements were performed on a Phillips X'Pert Pro MPD diffractometer in the 2θ range of 20–90°. Low temperature analysis was performed using a PANAlytical Empyrean diffractometer, equipped with an Oxford Cryostat PheniX camera, upon cooling from 20 to -150 °C with a 50 °C step and then upon heating. The obtained XRD patterns

were analyzed by Rietveld refinement, as implemented in the FullProf software suite [19]. Starting models were based on the monoclinic fergusonite ($I2/c$) [20] and tetragonal scheelite ($I4_1/a$) [21] structures of $LaNbO_4$. Rietveld refinement was performed with a Pseudo-Voigt and axial divergence asymmetry function. The calculations of spontaneous strain and Landau order parameter were performed on the theoretical basis described in our previous research on doped lanthanum orthoniobates [4, 14].

Powder neutron diffraction data were collected on the Polaris diffractometer at the ISIS Facility, Rutherford Appleton Laboratory. Data collected on back-scattering (average angle 146.72°) and 90° (average angle 92.5°) detector banks were used in subsequent refinements. Room temperature data were collected with the sample contained in a cylindrical 11 mm diameter thin walled vanadium can, located in front of the back-scattering detectors. Data collections of 1000 μA h were made at room temperature. Structure refinement was carried out by conventional Rietveld analysis using the GSAS software package [22]. The models of David [21] and Tsunekawa et al. [20] for $LaNbO_4$ were used as starting models for the tetragonal and monoclinic phases, respectively.

X-ray absorption spectroscopy (XAS) was performed at the Elettra Sinchrotrone XAFS beamline (Trieste, Italy). High quality XAFS spectra of the La and Sb L_3-edges (5483 eV and 4132 eV, respectively) and at the Nb K-edge (18986 eV) were collected. Measurements were performed at room temperature using transmission geometry. Because of the low antimony content, Sb L_3 spectra collection

required longer acquisition time (than in the case of other edges) and each scan was repeated at least twice. Obtained XANES spectra were normalized by subtracting the pre-edge background (fitted linearly) from all points and dividing the difference by the absorption jump.

Powders of antimony doped lanthanum orthoniobate were characterized using X-ray photoelectron spectroscopy (XPS). The spectra were recorded on a Thermo Scientific K-Alpha+ X-ray photoelectron spectrometer system operating at a base pressure of 2×10^{-9} mbar. The system incorporates a monochromatic, microfocused Al Kα X-ray source (hν = 1486.6 eV) and a 180° double focusing hemispherical analyzer with a 2D detector. The X-ray source was operated at 6 mA emission current and 12 kV anode bias and an X-ray spot size of 400 μm was used. Data were collected at pass energies of 200 eV for survey scans and 20 eV for core level spectra. A flood gun was used to minimize sample charging. Spectra were aligned assuming the C 1*s* core line to be at the binding energy of 284.8 eV. All data were analyzed using the Avantage software package.

3. Results and discussion

3.1 X-ray diffraction

The results of X-ray diffraction experiments, performed at room temperature, confirm that all of the specimens can be indexed as lanthanum orthoniobate (either

monoclinic $I2/c$ and/or tetragonal $I4_1/a$). $LaNb_{0.9}Sb_{0.1}O_{4-\delta}$ and $LaNb_{0.75}Sb_{0.25}O_{4-\delta}$ exhibit the monoclinic fergusonite structure, whereas in the case of $LaNb_{0.7}Sb_{0.3}O_{4-\delta}$ the tetragonal scheelite constitutes the majority phase. Figure 1 shows the thermal evolution of the X-ray diffraction pattern of $LaNb_{0.7}Sb_{0.3}O_{4-\delta}$ on cooling and heating. The structural phase transition between the low-temperature fergusonite ($I2/c$) and the high-temperature scheelite ($I4_1/a$) structure takes place at temperatures between 10 °C and 20 °C. The temperature evolution of unit cell parameters determined from Rietveld refinement, depicted in Figure 2a, is typical of the system and was previously observed in other orthoniobates [4, 7, 10, 14, 23]. A decrease of monoclinic angle with increasing temperature is characteristic of the approaching phase transition. In $LaNb_{0.7}Sb_{0.3}O_4$ the monoclinic angle achieves 90° between 10 °C and 20 °C. This is consistent with the trend of decreasing phase transition temperature obtained from results of dilatometry measurements for $LaNb_{1-x}Sb_xO_4$ for x between 0.05 and 0.25 in our previous study [7], which indicated that the transition temperature of $LaNb_{0.7}Sb_{0.3}O_4$ should be close to room temperature. Figures 1 and 2 show that the monoclinic fergusonite and tetragonal scheelite phases co-exist in $LaNb_{0.7}Sb_{0.3}O_4$ over a wide temperature range. The co-existence of two phases in lanthanum orthoniobates has been previously reported by us for antimony and magnesium substitution [7, 14] and by other groups for calcium substitution.

Figure 2 b presents the dependence of scalar spontaneous strain on temperature as well as on Landau's order parameter defined as $\sqrt{\frac{T_0-T}{T_0}}$, where T_0 is the

transition temperature. The transition temperature was assumed to be 15±5 °C. The values of scalar spontaneous strain were calculated on the basis of the unit cell parameters [14]. The relation between the scalar spontaneous strain, temperature and Landau's order parameter shows that the 30 mol% substituted material behaves similarly to $LaNb_{0.75}Sb_{0.25}O_{4-\delta}$ and $LaNb_{0.9}Sb_{0.1}O_{4-\delta}$ reported previously, however the strain values in $LaNb_{0.7}Sb_{0.3}O_{4-\delta}$ are lower [4]. This result also supports those from previous studies showing that in the case of the lanthanum orthoniobate system the phase transition is second order (linear relation of Landau's order parameter and spontaneous strain) [6, 14].

The structural phase transition that occurs in the lanthanum orthoniobate system is one of the main features that limited application of these materials. This transition is accompanied by a rapid change in thermal expansion coefficient (from 12 to 8×10^{-6} K^{-1}) which can result in delamination and device failure [14]. The suppression of this transition, to temperatures below 20 °C, through isovalent substitution makes application of these materials more feasible.

3.2 Neutron diffraction

Neutron diffraction studies were undertaken for samples with 10, 25 and 30 mol% of antimony. The data for $LaNb_{0.75}Sb_{0.25}O_{4-\delta}$ and $LaNb_{0.7}Sb_{0.3}O_{4-\delta}$ showed significant *hkl* dependent broadening. This is probably related to the vicinity of the structural phase transition. The peak broadening may also be caused by the structural strain caused by the ionic radii difference between Sb^{5+} and Nb^{5+} (the ionic radii of Sb^{5+} and Nb^{5+} for

six-fold coordination are 0.6 Å and 0.64 Å, respectively [24]). The unit cell and refinement parameters from the room temperature refinements are summarised in Table 1 with refined structural parameters and selected contact distances given in the supporting information (Supplementary information Tables S1 to S3) along with the fitted diffraction profiles (Figures S1-S3). The data for the sample substituted by 10 mol% of antimony were fitted solely with the monoclinic structure ($I2/c$), while those for the 30 mol% sample were fitted with the tetragonal ($I4_1/a$) phase only. In the case of 25 mol% substitution, the profile was fitted with a multiphase model containing both monoclinic and tetragonal phases and revealed a phase content ratio of approximately 0.87/0.13 w/w (see Table 1). The unit cell parameters are consistent with those obtained previously on the basis of XRD analysis [4]. The refined oxygen occupancy for all investigated compositions shows extremely low oxygen vacancy concentrations at room temperature ($\delta \approx 0$). This is in agreement with previous high temperature ND studies undertaken by Malavasi et al. on the acceptor doped system $La_{0.99}Ca_{0.01}NbO_4$ [23].

The Nb/Sb-O bond lengths of the majority phase decreased with increasing antimony content, reflecting the smaller ionic radius of Sb^{5+} in relation to Nb^{5+}. However, the total change in the volume of the tetrahedra is small (~0.04 $Å^3$ between 25 and 30 mol% of antimony). On the other hand, the average length of the La-O bonds tends to increase with increasing antimony content.

3.3 X-ray absorption spectroscopy (XAS)

Figures 3 - 5 present the results of X-ray absorption studies for the Sb L_3-edge, Nb K-edge, and La L_3-edge spectra, respectively. Samples were analyzed both before and after protonation. Figure 3 depicts the antimony L_3 normalized XANES data together with the L_3 XANES of Sb_2O_3. One can note that in the spectra of $LaNb_{1-x}Sb_xO_{4-\delta}$ neither the pre-peak nor white line (WL) characteristic of the Sb^{3+} species are visible (Fig. 3). The positions of both pre-peak (4135.5 eV) and L_3-edge (4145 eV) are independent of Sb content and are attributed solely to Sb^{5+} species, which according to Kilias et al. in the spectra of $Fe^{3+}Sb^{5+}O_4$ are located at ~4135 eV and ~4144 eV, respectively [25]. This confirms our previous conclusions, based on electrical and thermal studies, that antimony in the lanthanum orthoniobate structure maintains an oxidation state of 5+ [4, 5]. In this study we confirm that higher oxidation state of antimony in lanthanum orthoniobate is maintained in the bulk material not just at the surface.

In Figure 4, X-ray absorption near-edge spectroscopy results (normalized XANES) in the range of the Nb K-edge are shown for all compositions and compared with the standards for Nb^{4+} (NbO_2) and Nb^{5+} (Nb_2O_5). Comparison with the standards reveals that niobium is in the 5+ oxidation state. This is consistent with the XPS niobium 3*d* core level spectra (Figure S4) and the neutron diffraction results that indicate no oxygen vacancies. The resonance in the pre-edge region of Nb K-edge spectra, at around 18990 eV, can be assigned to the transition of the 1*s* electron to the 4*d* state, which is forbidden in compounds with inversion symmetry due to the dipole

selection rule. The non-centrosymmetric positions of the Nb and La atoms in the oxygen tetrahedra lead to hybridization of the Nb 4*d* with the O 2*p* atomic orbitals, introducing *p* character to the *d* type molecular orbitals, a phenomenon previously reported for $LiNbO_3$ [26, 27]. Moreover, increasing pre-peak intensity with increasing Sb content implies a decrease in local structure disorder viewed rather as a higher ordering in O-Nb-O angular distribution than in Nb-O length distribution [28]. An additional visible effect is the white line splitting at the Nb K-edge, which is probably due to splitting of the 5*p* state [27]. This behavior is visible for all investigated samples. Figures 4a and 4b show that the splitting becomes smaller for larger Sb content and the protonation does not affect this phenomenon.

In Figure 5, the X-ray absorption spectra measured around the La L_3-edge are shown. Lanthanum L_3 normalized XANES spectra for all studied $LaNb_{1-x}Sb_xO_{4-\delta}$ ceramics and reference samples are presented. It can be noted that edge position is independent of Sb content, indicating the same formal charge for La in all studied samples. The white line (WL) deconvolution shows a well distinguished single peak at approximately 5490 eV (see inset in Fig. 5). Asakura et al. calculated the relations between WL intensities, their full width at half maximum (FHWM), and average coordination numbers for multiple lanthanum oxides [29]. Figure 5c presents the WL FWHM as a function of the substituent content. The value for lanthanum oxide has been added to the figure for comparison. The results could suggest the change in coordination of lanthanum cations within the structure changing from 7 for unsubstituted to 8-9 for substituted samples. However, the neutron diffraction results

show 8-fold coordination of lanthanum for all investigated samples. Therefore, one can assume that the subtle changes observed in lanthanum WL shape can be attributed in this case not to varying coordination, but to small changes in bond lengths and angles between lanthanum and coordinated oxygens. Figure 5d shows the changes in the WL normalized intensity of the La L_3-edge with antimony content. One can see, that with increasing antimony content the WL intensity rises with a decrease of the line width (*d*-state broadening), indicating that the charge distribution around La^{3+} ions becomes more localized. This points to local structure changes, in particular in bond lengths, and can be supported by use of a bond-valence model. The bond-valence model predicts the ideal atomic bond length R_{ij} between atoms in inorganic solids through the relation with average valence states as described in (eq. 2).

$$s_{ij} = \exp\left(\frac{R_0 - R_{ij}}{B}\right) \qquad (2)$$

where the subscripts, *i* and *j*, refer to different atoms, $\sum_j s_{ij} = V_i$, and V_i is the atomic valence of atom *i*, R_0 and *B* are empirical parameters that must be fitted. Brown and Altermatt have reported values of R_0 for many common bonds, and have shown that *B* for most bonds can be set equal to 0.37 Å [30, 31]. One can note that the ideal bond lengths calculated in this model depend only on average atomic valences of given atoms and therefore on their coordination. If one assumes seven-fold coordination of lanthanum in the lanthanum orthoniobate unit cell, the ideal bond length is calculated as 2.48 Å, while for eight-fold coordination it is 2.53 Å. The structural data obtained by neutron diffraction (Table S1-S3) show that the average length of the La-O bond in the

majority phase increases from 2.502 ± 0.001 Å in $LaNb_{0.9}Sb_{0.1}O_{4-\delta}$ to only 2.507 ± 0.001 Å in $LaNb_{0.7}Sb_{0.3}O_{4-\delta}$. This suggests that in fact for lanthanum orthoniobate, the relation of WL intensity does not follow the trend of changing coordination, but the changes are an indication of subtle structural modification in bond lengths and angle distribution.

The comparison of the XANES Sb L_3-edge, Nb K-edge and La L_3-edge spectra obtained in the samples before and after protonation, displayed in Figures 3-5, shows that the influence of the presence of protonic defects in the materials on their electronic structure is subtle. Figure 3b presents a comparison of antimony L_3-edge for samples before and after protonation. One can see that both pre-peaks and WL shape and intensity are almost in every case independent of protonation. The influence of protonic defects on niobium XANES spectra is even weaker, there are no detectable differences in both niobium pre-peak and edge features for hydrated and non-hydrated specimens. This is observed for all compositions and is independent of the content of antimony (Fig. 4b). However, a visible influence of protonation on the La L_3 WL intensity and FWHM may be seen in the case of samples with Sb content higher than 25 mol% (Fig. 5c and 5d). When changing Sb content from 25 mol% to 30 mol%, an increase in WL FWHM for the protonated samples is accompanied by a decrease in the normalized intensity, suggesting that with increasing protonic defect concentration, the distortion of coordination environment of lanthanum decreases as does the density of unoccupied electronic states.

Summing up, the influence of protonic defects is limited to the electronic structure of the La^{3+} cations in samples with higher antimony content. This may be caused by low proton concentration in the samples with smaller antimony content, as shown by thermogravimetry in our previous study [18]. The influence of protonic defects on niobium and antimony is quite negligible with respect to the changes observed for lanthanum. This is an interesting feature taking into consideration that, according to Fjeld et al. [16], the most stable proton site in tetragonal lanthanum orthoniobate is the one between two neighbouring NbO_4 tetrahedra and not the one between neighbouring lanthanum atoms, since the energy difference between these sites is 0.13 eV. A similar relationship was found for monoclinic $LaNbO_4$ [16].

Summing up, The obtained results indicate that the formal charges of all analyzed elements in the studied compounds are stable and Sb content is independent (at least in the considered range of substitution). However, the antimony substitution as well as protonation changed the density of unoccupied electron states around lanthanum.

3.4 X-ray photoelectron spectroscopy (XPS)

Valence band X-ray photoelectron spectroscopy was used to determine the position of the valence band maximum E_{VBM} relative to the Fermi energy E_F at the sample surface. Figure 6 presents XPS data for the valence band (VB) region of three different compositions of $LaNb_{1-x}Sb_xO_{4-\delta}$, where x = 0.1, 0.2, 0.3. The E_{VBM} positions relative to E_F were determined using linear fitting of the valence band maximum (VBM) and the

background. Within the errors of the measurements no difference could be detected and a value of 2.4±0.1 eV was extracted for all three samples. Thus, E_{VBM} does not change relative to E_F with increasing antimony content.

The ionization potential (IP) can be obtained from the difference between the vacuum potential (V_{vac}) and the energy of the highest occupied Kohn-Sham orbital defined, as simulations suggest, as the valence band maximum ($IP = V_{vac} - E_{VBM}$) [32]. From the point of view of charge equilibrium, proton addition and electron removal from the structure are equivalent processes, and it is known from other studies, that the IP values may correlate with proton affinity [33]. For example, in multiple oxygen-containing molecules a linear relation between these two parameters was found [34]. A constant E_{VBM} value maybe be surprising, considering the higher protonation of samples with higher dopant content reported previously [18]. However, this suggests that the rise in conductivity observable for compositions with higher Sb content is solely related to charge mobility, not to affinity to water incorporation within the structure [18, 35].

4. Conclusions

Lanthanum orthoniobates substituted by antimony have been analyzed by means of X-ray and neutron diffraction, and X-ray absorption and X-ray photoelectron spectroscopy. The structure evolution upon heating and cooling for the sample with 30 mol% of antimony was analyzed in the temperature range from -150 to 50 °C by X-ray diffraction. The structural transition temperature between fergusonite and

scheelite phases was found to be 15 °C. It was shown that the addition of antimony decreases the spontaneous strain in the monoclinic phase.

Neutron diffraction studies show that niobium substitution by antimony influences the environment and properties of lanthanum-oxygen polyhedra to a small extent. The average length of La-O bonds slightly increases. Oxygen non-stoichiometry was found to be very low. This significantly lowers the degree of hydration possible in these systems.

Protonic defects were found to influence the electronic structure of La^{3+} cations in samples with high antimony content, but not Sb^{5+} or Nb^{5+} cations. The presence of protonic defects was found to decrease the density of unoccupied electronic states. No influence of antimony on the position of the valence band maximum was observed.

$LaNb_{0.7}Sb_{0.3}O_4$ shows a pure scheelite phase at room temperature. Despite its low hydration level, this composition exhibits high protonic conductivity, as well as a better matched thermal expansion coefficient making it well suited for application in protonic ceramic electrochemical cells.

5. **Acknowledgements**

A.M.-G. and S.W. acknowledge support from the Ministry of Science and Higher Education, Poland Grant No IP2015 051374. The authors acknowledge the CERIC-

ERIC Consortium for access to the Elettra Sinchrotrone Trieste and for financial support under proposal 20177009. The authors are grateful to the STFC ISIS Facility for a neutron beam time award (RB 63849) and to Dr Ron Smith at ISIS for his help in data collection. D.J.P and A.M.-G. ackowlegde support from Solid Oxide Interfaces for Faster Ion Transport JSPS Core-to-Core Program (Advanced Research Networks).

6. References

1. Mielewczyk-Gryn A, Gdula K, Lendze T, Kusz B, Gazda M. Nano- and microcrystals of doped niobates. *Cryst Res Technol*. 2010;45(12):1225–1228. https://doi.org/10.1002/crat.201000378

2. Mokkelbost T, Lein HL, Vullum PE, Holmestad R, Grande T, Einarsrud M-A. Thermal and mechanical properties of LaNbO4-based ceramics. *Ceram Int*. 2009;35(7):2877–2883. https://doi.org/10.1016/j.ceramint.2009.03.041

3. Prytz O, Tafto J. Accurate determination of domain boundary orientation in LaNbO4. *Acta Mater*. 2005;53(2):297–302. https://doi.org/10.1016/j.actamat.2004.09.023

4. Mielewczyk-Gryn A, Wachowski S, Lilova KII, Guo X, Gazda M, Navrotsky A. Influence of antimony substitution on spontaneous strain and thermodynamic stability of lanthanum orthoniobate. *Ceram Int*. 2015;41(2):2128–2133. https://doi.org/10.1016/j.ceramint.2014.10.010

5. Wachowski S, Mielewczyk-Gryń A, Zagórski K, *et al.* Influence of Sb-substitution

on ionic transport in lanthanum orthoniobates. *J Mater Chem A*. 2016;4(30):11696–11707. https://doi.org/10.1039/C6TA03403A

6. Mielewczyk-Gryn A, Wachowski S, Strychalska J, *et al.* Heat capacities and thermodynamic properties of antimony substituted lanthanum orthoniobates. *Ceram Int*. 2016;42(6):7054–7059. https://doi.org/10.1016/j.ceramint.2016.01.093

7. Wachowski S, Mielewczyk-Gryn A, Gazda M. Effect of isovalent substitution on microstructure and phase transition of LaNb1-xMxO4 (M=Sb, v or Ta; X=0.05-0.3). *J Solid State Chem*. 2014;219:201–209. https://doi.org/10.1016/j.jssc.2014.07.041

8. Brandão AD, Antunes I, Frade JR, Torre J, Kharton V V., Fagg DP. Enhanced Low-Temperature Proton Conduction in Sr 0.02 La 0.98 NbO 4−δ by Scheelite Phase Retention. *Chem Mater*. 2010;22(24):6673–6683. https://doi.org/10.1021/cm102705e

9. Aldred AT, Chan S-K, Grimsditch MH, Nevitt M V. Displacive Phase Transformation in Vanadium - Substituted Lanthanum Niobate. *MRS Proc*. 1983;24:81. https://doi.org/10.1557/PROC-24-81

10. Wachowski S, Kamecki B, Winiarz P, Dzierzgowski K, Mielewczyk-Gryń A, Gazda M. Tailoring structural properties of lanthanum orthoniobates through an isovalent substitution on the Nb-site. *Inorg Chem Front*. 2018;5(9):2157–2166.

https://doi.org/10.1039/C8QI00524A

11. Bi Z, Bridges CA, Kim J-H, Huq A, Paranthaman MP. Phase stability and electrical conductivity of Ca-doped LaNb1−xTaxO4−δ high temperature proton conductors. *J Power Sources*. 2011;196(18):7395–7403. https://doi.org/10.1016/j.jpowsour.2011.04.006

12. Santibáñez-Mendieta AB, Fabbri E, Licoccia S, Traversa E. Tailoring phase stability and electrical conductivity of Sr0.02La0.98Nb1–xTaxO4 for intermediate temperature fuel cell proton conducting electrolytes. *Solid State Ionics*. 2012;216:6–10. https://doi.org/10.1016/j.ssi.2011.09.019

13. Vullum F, Nitsche F, Selbach SM, Grande T. Solid solubility and phase transitions in the system LaNb1−xTaxo4. *J Solid State Chem*. 2008;181(10):2580–2585. https://doi.org/10.1016/j.jssc.2008.06.032

14. Mielewczyk-Gryn A, Gdula-Kasica K, Kusz B, Gazda M. High temperature monoclinic-to-tetragonal phase transition in magnesium doped lanthanum ortho-niobate. *Ceram Int*. 2013;39(4):4239–4244. https://doi.org/10.1016/j.ceramint.2012.09.102

15. Løken A, Ricote S, Wachowski S. Thermal and Chemical Expansion in Proton Ceramic Electrolytes and Compatible Electrodes. *Crystals*. 2018;8(9):365. https://doi.org/10.3390/cryst8090365

16. Fjeld H, Toyoura K, Haugsrud R, Norby T. Proton mobility through a second

order phase transition: theoretical and experimental study of LaNbO4. *Phys Chem Chem Phys*. 2010;12(35):10313–9. https://doi.org/10.1039/c002851g

17. Nevitt M, Knapp G. Phonon properties of vanadium-substituted lanthanum niobate derived from heat-capacity measurements. *J Phys Chem Solids*. 1986;47(5):501–505.

18. Mielewczyk-Gryń A, Wachowski S, Prześniak-Welenc M, *et al.* Water uptake analysis of acceptor-doped lanthanum orthoniobates. *J Therm Anal Calorim*. 2019. https://doi.org/10.1007/s10973-019-08208-6

19. Rodríguez-carvajal J. Recent developments for the program FULLPROF. 2001

20. Tsunekawa S, Takei H, Ishigame M. Study on the room temperature phase of LaNbO4 crystals. *Mater Res Bull*. 1977;12(11):1087–1094. https://doi.org/10.1016/0025-5408(77)90037-X

21. David WIF. The high-temperature paraelastic structure of LaNbO4. *Mater Res Bull*. 1983;18(6):749–756. https://doi.org/10.1016/0025-5408(83)90103-4

22. Soediono B. General Structure Analysis System. *J Chem Inf Model*. 1989;53:160. https://doi.org/10.1017/CBO9781107415324.004

23. Malavasi L, Ritter C, Chiodelli G. Investigation of the high temperature structural behavior of La0.99Ca0.01NbO4 proton conducting material. *J Alloys Compd*. 2009;475(1–2):L42–L45. https://doi.org/10.1016/j.jallcom.2008.08.032

24. Shannon RD, Prewitt CT. Effective ionic radii in oxides and fluorides. *Acta Crystallogr Sect B Struct Crystallogr Cryst Chem*. 1969;25(5):925–946. https://doi.org/10.1107/S0567740869003220

25. S.P. Kilias, M. Gousgouni A, Godelitsas, P. Gamaletsos, T.J. Mertzimekis P, Nomikou, A. Argyraki, J. Goettlicher RS, Papanikolaou D. ANTIMONY FIXATION IN SOLID PHASES AT THE HYDROTHERMAL FIELD OF KOLUMBO SUBMARINE ARC-VOLCANO (SANTORINI): DEPOSITION MODEL AND ENVIRONMENTAL IMPLICATIONS. *Bull Geplogica Soc Greece*. 2016;50(2010):656–664. https://doi.org/http://dx.doi.org/10.12681/bgsg.14276

26. Hafid L, Michel-Calendini FM. Electronic structure of linb03: Densities of states, optical anisotropy and spontaneous polarisation calculated from the xa molecular orbital method. *J Phys C Solid State Phys*. 1986;19(16):2901–2917. https://doi.org/10.1088/0022-3719/19/16/011

27. Vitova T. X-ray absorption spectroscopy investigation of structurally modified lithium niobate crystals. UNIVERSITAT BONN; 2003

28. Asakura H, Shishido T, Yamazoe S, Teramura K, Tanaka T. Structural Analysis of Group V, VI, and VII Metal Compounds by XAFS. *J Phys Chem C*. 2011;115(48):23653–23663. https://doi.org/10.1021/jp2034104

29. Asakura H, Shishido T, Teramura K, Tanaka T, Japan T. Local Structure and La L1 and L3-Edge XANES Spectra of Lanthanum Complex Oxides. *Inorg Chem*.

2014;53. https://doi.org/10.1021/ic500381z

30. Brown ID, D.Altermatt. Bond-Valence Parameters Obtained from a Systematic Analysis of the Inorganic Crystal Structure Database I . D . B R O W N A N D D . A L T E R M A T F The bond file produced from the Inorganic Crystal. *Acta Crystallogr Sect B*. 1985;244(2):244–247. https://doi.org/10.1107/S0108768185002063

31. Brown ID, IUCr. Chemical and steric constraints in inorganic solids. *Acta Crystallogr Sect B Struct Sci*. 1992;48(5):553–572. https://doi.org/10.1107/S0108768192002453

32. Jiang H, Shen YC. Ionization potentials of semiconductors from first-principles. *J Chem Phys*. 2013;139(16). https://doi.org/10.1063/1.4826321

33. Bjørheim TS, Hoedl MF, Merkle R, Kotomin EA, Maier J. Proton, Hydroxide Ion, and Oxide Ion Affinities of Closed-Shell Oxides: Importance for the Hydration Reaction and Correlation to Electronic Structure. *J Phys Chem C*. 2019;acs.jpcc.9b07570. https://doi.org/10.1021/acs.jpcc.9b07570

34. BENOIT FM, HARRISON AG. PREDICTIVE VALUE OF PROTON AFFINITY. IONIZATION ENERGY CORRELATIONS INVOLVING OXYGENATED MOLECULES. *J Am Chem Soc*. 1977;99(12):3980–3984. https://doi.org/10.1021/ja00454a015

35. Wachowski S, Mielewczyk-Gryń A, Zagórski K, *et al.* Influence of Sb-substitution

on ionic transport in lanthanum orthoniobates. *J Mater Chem A*. 2016;4(30):11696–11707. https://doi.org/10.1039/C6TA03403A

Table 1. Crystal and refinement parameters for $LaNb_{1-x}Sb_xO_{4-\delta}$ at 20 °C. Estimated standard deviations are given in parentheses

Sample	x = 0.10	x = 0.25	x = 0.30
Temperature	20 °C	20 °C	20 °C
Chemical formula	$LaNb_{0.9}Sb_{0.1}O_{4-\delta}$	$LaNb_{0.75}Sb_{0.25}O_{4-\delta}$	$LaNb_{0.7}Sb_{0.30}O_{4-\delta}$
Formula weight	298.694 g mol^{-1}	303.02 g mol^{-1}	304.46 g mol^{-1}
Crystal system	Monoclinic	Phase 1 = Monoclinic Phase 2 = Tetragonal	Tetragonal
Space group	$I2/c$	Phase 1 = $I2/c$ Phase 2 = $I4_1/a$	$I4_1/a$
Lattice parameters	a = 5.55142(9) Å b = 11.5553(1) Å c = 5.2234(3) Å β = 93.553(1)°	Phase 1: a = 5.4785(2) Å b = 11.6189(2) Å c = 5.3056(5) Å β = 91.710(1)° Phase 2: a = 5.3938(6) Å c = 11.609(2) Å	a = 5.3994 (3) Å c = 11.636(1) Å
Volume	334.43(2) Å^3	Phase 1 = 337.58(4) Å^3 Phase 2 = 337.73(8) Å^3	339.23(6) Å^3
Z	4	Phase 1 = 4 Phase 2 = 4	4
Density (calc)	5.927 Mg m^{-3}	Phase 1 = 5.962 Mg m^{-3} Phase 2 = 5.959 Mg m^{-3}	5.958 Mg m^{-3}
Weight fraction	100	Phase 1 = 0.869(6) Phase 2 = 0.131(6)	100
R-factors[a]	(a) Neut. backscatter. R_{wp} = 0.0130 R_p = 0.0266 R_{ex} = 0.0030 R_{F^2} = 0.0516 (b) Neut. 90° R_{wp} = 0.0155 R_p = 0.0318 R_{ex} = 0.0026 R_{F^2} = 0.0455	(a) Neut. backscatter. R_{wp} = 0.0201 R_p = 0.0420 R_{ex} = 0.0033 R_{F^2} = 0.0229 (b) Neut. 90° R_{wp} = 0.0180 R_p = 0.0319 R_{ex} = 0.0028 R_{F^2} = 0.0206	(a) Neut. backscatter. R_{wp} = 0.0244 R_p = 0.0437 R_{ex} = 0.0032 R_{F^2} = 0.0914 (b) Neut. 90° R_{wp} = 0.0252 R_p = 0.0314 R_{ex} = 0.0027 R_{F^2} = 0.0362
No. of variables	129	146	111
No of profile points used	3408 (neut. backscatter.) 2591 (neut. 90°)	2910 (neut. backscatter.) 2409 (neut. 90°)	3368 (neut. backscatter.) 2439 (neut. 90°)

[a]For definition of R-factors see reference 23

Figure captions

Figure 1. X-ray diffraction patterns for $LaNb_{0.7}Sb_{0.3}O_{4-\delta}$ collected upon (a) cooling and (b) heating.

Figure 2. (a) Temperature dependence of the phase content and unit cell parameters of fergusonite (m) and scheelite (t) phases of $LaNb_{0.7}Sb_{0.3}O_{4-\delta}$, based on refinement of the data collected upon cooling. (b) Scalar spontaneous strain plotted as a function of temperature and Landau's order parameter for $LaNb_{0.7}Sb_{0.3}O_{4-\delta}$.

Figure 3. Sb L_3-edge normalized XANES spectra obtained for (a) the $LaNb_{1-x}Sb_xO_{4-\delta}$ ceramics and reference sample and (b) samples before and after protonation. In the insets, the first derivatives of the edge range are presented.

Figure 4. Nb K-edge normalized XANES spectra obtained for (a) all studied $LaNb_{1-x}Sb_xO_{4-\delta}$ ceramics and reference samples and (b) studied ceramics before and after protonation. In the insets the first derivatives of the edge range are presented.

Figure 5. La L_3-edge normalized XANES spectra obtained for (a) the $LaNb_{1-x}Sb_xO_{4-\delta}$ ceramics and reference samples, (in the inset example WL decomposition is shown); (b) the samples before and after protonation; (c) FWHM of lanthanum L_3-edge white line versus antimony content for measured samples (the value for La_2O_3 is presented for comparison and the dashed line is a guide to the eye, coordination numbers were attributed according to Asakura et al. [29] and (d) lanthanum L_3-edge white line intensity versus *x* for the samples before and after protonation.

Figure 6. XPS valence band spectra for $LaNb_{1-x}Sb_xO_{4-\delta}$. Red lines indicate linear fits to the valence band maximum (VBM) and background to determine the VBM position.

Supplementary figures captions

Figure S1 Fitted neutron diffraction profiles for $LaNb_{0.9}Sb_{0.1}O_{4-\delta}$ showing data from (a) neutron back scattering and (b) 90° detector banks. Observed (+ symbols), calculated (line) and difference (lower) profiles are shown with reflection positions indicated by markers.

Figure S2 Fitted neutron diffraction profiles for $LaNb_{0.75}Sb_{0.25}O_{4-\delta}$ showing data from (a) neutron back scattering and (b) 90° detector banks. Observed (+ symbols), calculated (line) and difference (lower) profiles are shown with reflection positions indicated by markers (lower: phase 1 and upper: phase 2).

Figure S3 Fitted neutron diffraction profiles for $LaNb_{0.7}Sb_{0.3}O_{4-\delta}$ showing data from (a) neutron back scattering and (b) 90° detector banks. Observed (+ symbols), calculated (line) and difference (lower) profiles are shown with reflection positions indicated by markers.

Figure S4 X-ray photoelectron spectra of investigates samples lanthanum, niobium and antimony core-shell.

Supporting Information

Diffraction and spectroscopic studies of antimony substituted lanthanum orthoniobate

Aleksandra Mielewczyk-Gryń, Sebastian Wachowski, Agnieszka Witkowska, Kacper Dzierzgowski, Wojciech Skubida, Konrad Świerczek, Anna Regoutz, David J. Payne, Stephen Hull, Hangfeng Zhang, Isaac Abrahams and Maria Gazda

(a)

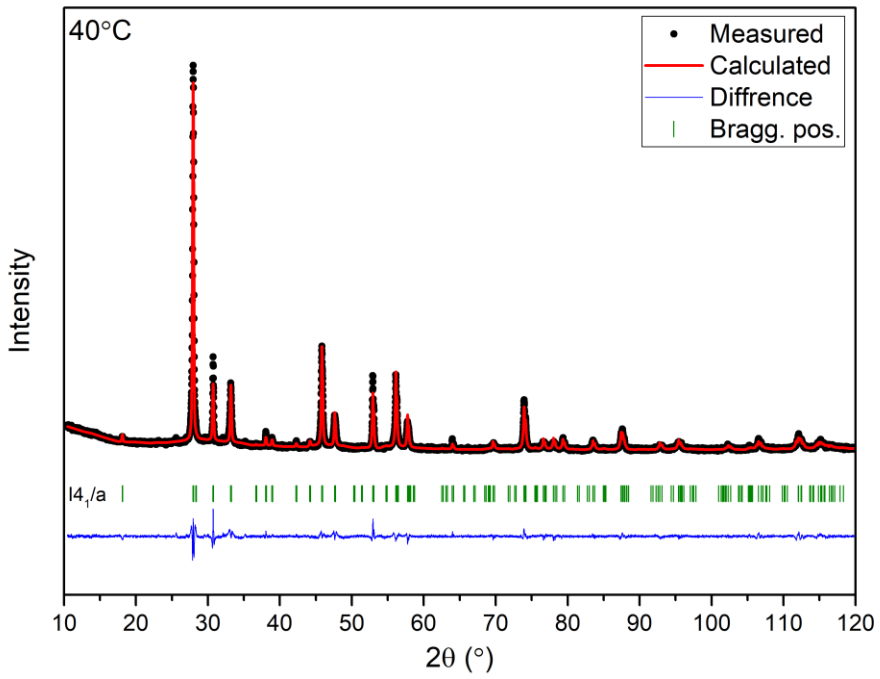

(b)

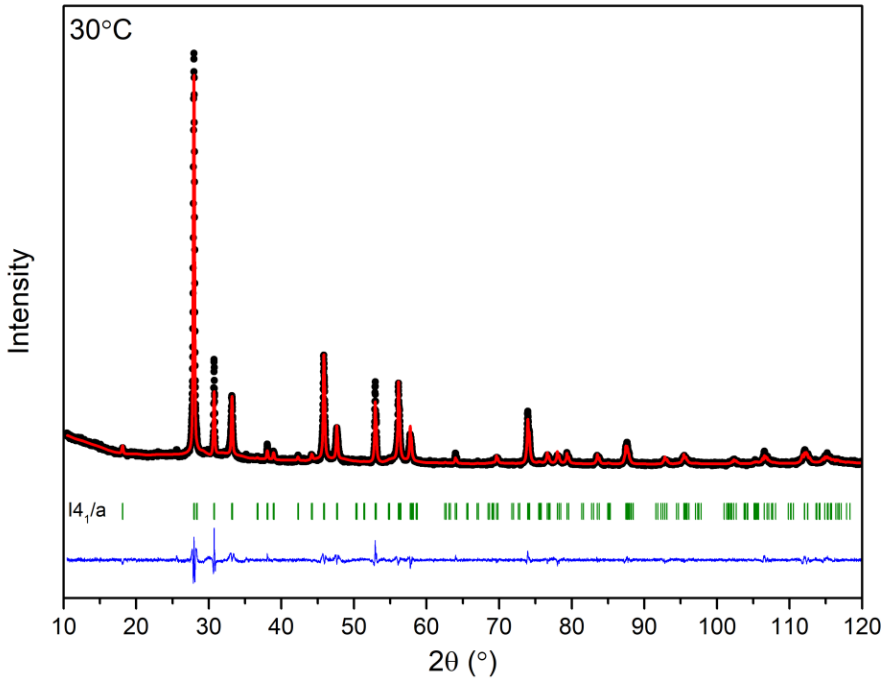
30°C
Intensity
I4₁/a
10
20
30
40
50
60
70
80
90
100
110
120
2θ (°)

(c)

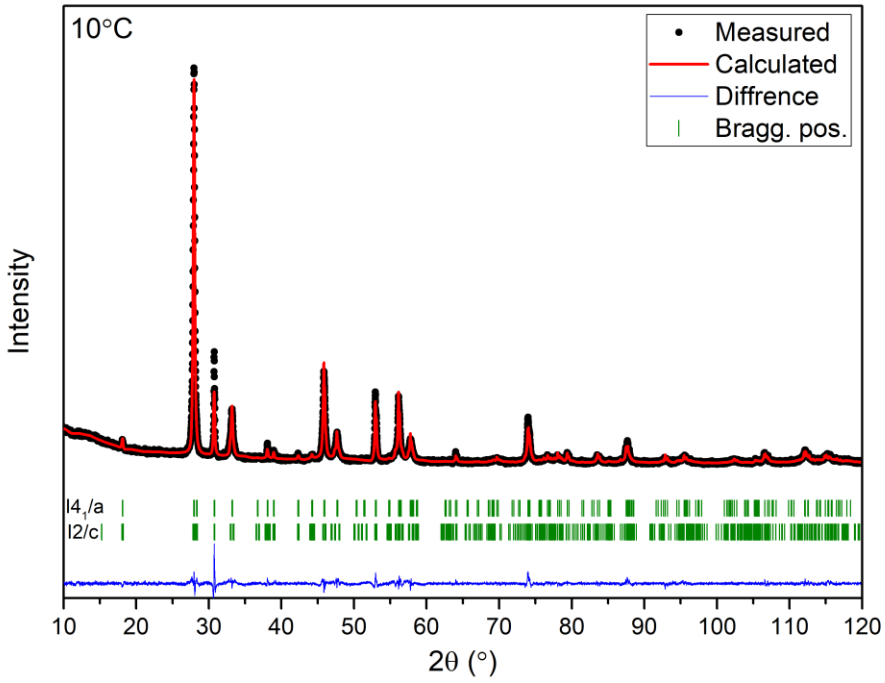
10°C
Measured
Calculated
Diffrence
Bragg. pos.
Intensity
I4₁/a
I2/c
10
20
30
40
50
60
70
80
90
100
110
120
2θ (°)

(d)

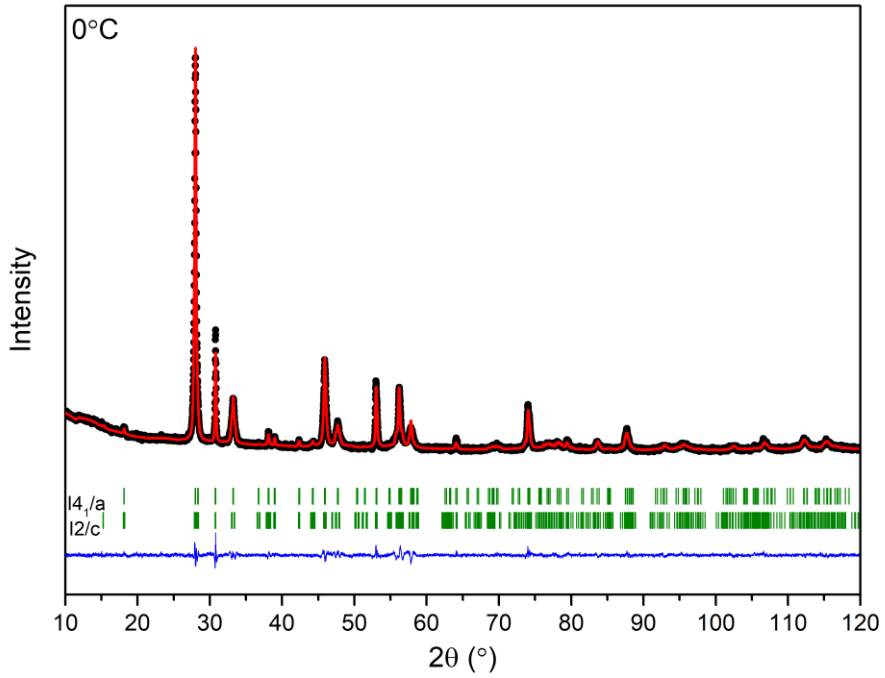
0°C
Intensity
I4₁/a
I2/c
10 20 30 40 50 60 70 80 90 100 110 120
2θ (°)

(e)

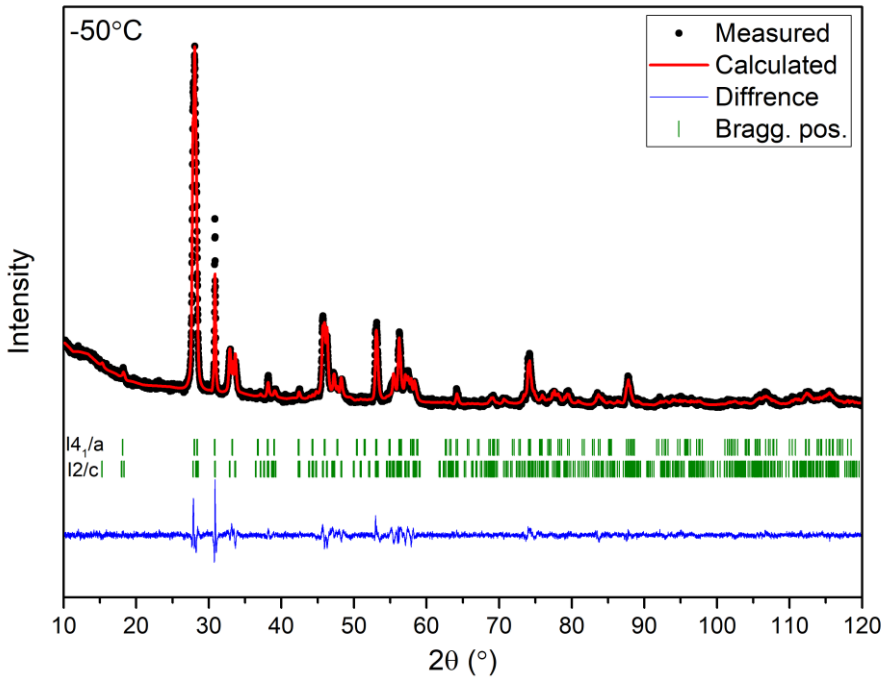
-50°C
Measured
Calculated
Diffrence
Bragg. pos.
Intensity
I4₁/a
I2/c
10 20 30 40 50 60 70 80 90 100 110 120
2θ (°)

(f)

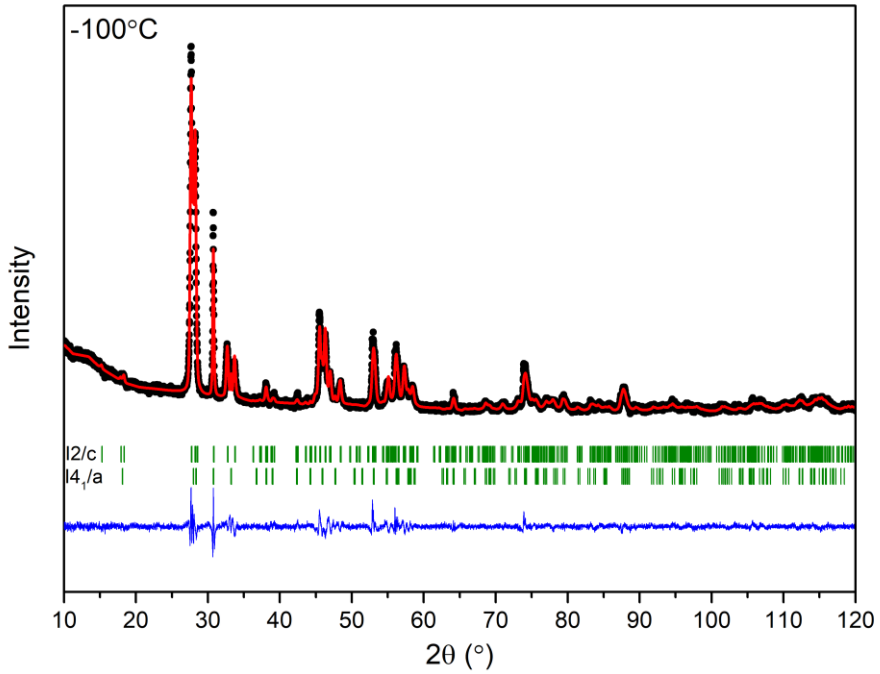
-100°C
Intensity
I2/c
I4$_1$/a
10 20 30 40 50 60 70 80 90 100 110 120
2θ (°)

(g)

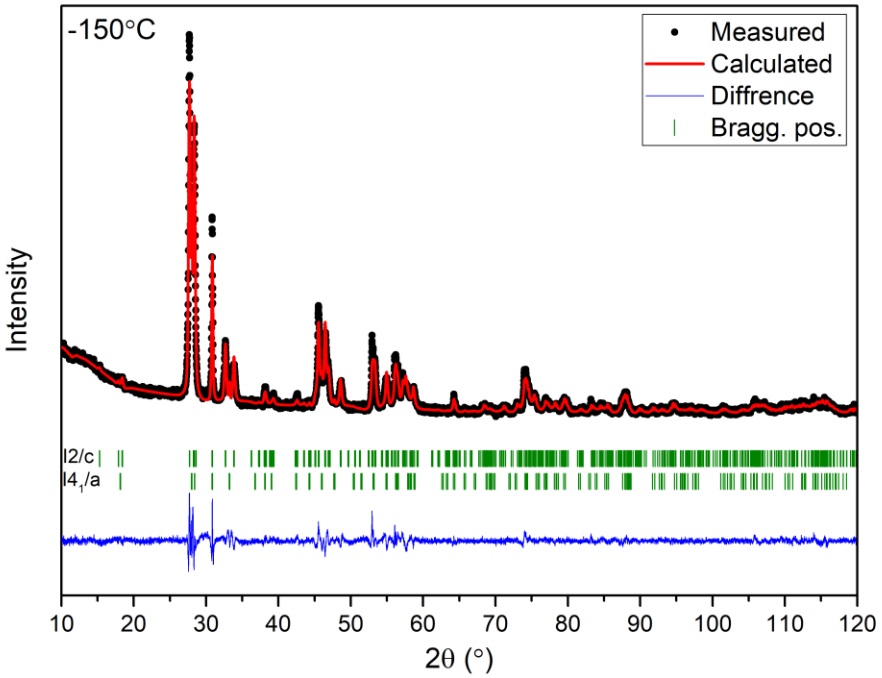
-150°C
Measured
Calculated
Diffrence
Bragg. pos.
Intensity
I2/c
I4$_1$/a
10 20 30 40 50 60 70 80 90 100 110 120
2θ (°)

Figure S1. Fitted X-Ray diffraction profiles for $LaNb_{0.7}Sb_{0.3}O_{4-\delta}$ showing data for temperatures (a) 40°C, (b) 30°C, (c) 10°C, (d) 0°C, (e) -50°C, (f) -100°C and (g) -150°C . Observed (• symbols), calculated (line) and difference (lower) profiles are shown with reflection positions indicated by markers.

Table S1. Crystal and refinement parameters calculated for $LaNb_{0.7}Sb_{0.3}O_{4-\delta}$ at 40°C, 30°C and 10°C calculated on the basis of X-Ray diffractograms. Estimated standard deviations are given in parentheses.

Temperature	40°C	30°C	10°C
Crystal system	Monoclinic	Monoclinic	Phase 1 = Monoclinic Phase 2 = Tetragonal
Space group	$I2/c$	$I2/c$	Phase 1 = $I2/c$ Phase 2 = $I4_1/a$
Lattice parameters	a = 5.3961 (1) Å c = 11.6339 (2) Å	a = 5.3960 (1) Å c = 11.6331 (2) Å	Phase 1: a = 5.4272 (1) Å b = 11.6234 (3) Å c = 5.3652 (1) Å β = 91.710(1)° Phase 2: a = 5.3939 (1) Å c = 11.6266 (2) Å
Volume	338.75 (2) Å^3	338.72 (3) Å^3	Phase 1 = 338.43 (4) Å^3 Phase 2 = 338.28 (2) Å^3
Density (calc)	5.970 Mg m^{-3}	5.970 Mg m^{-3}	Phase 1 = 5.978 Mg m^{-3} Phase 2 = 5.978 Mg m^{-3}
Weight fraction	100	100	Phase 1 = 0.393(9) Phase 2 = 0.607(7)
R-factors	R_{wp} = 17.8 R_p = 24.8 R_{ex} = 8.53	R_{wp} = 18.3 R_p = 25.8 R_{ex} = 8.71	R_{wp} = 16.6 R_p = 24.2 R_{ex} = 3.61

Table S2. Crystal and refinement parameters calculated for $LaNb_{0.7}Sb_{0.3}O_{4-\delta}$ at 0°C, -50°C and -100°C calculated on the basis of X-Ray diffractograms. Estimated standard deviations are given in parentheses.

Temperature	0°C	-50°C	-100°C
Crystal system	Phase 1 = Monoclinic Phase 2 = Tetragonal	Phase 1 = Monoclinic Phase 2 = Tetragonal	Phase 1 = Monoclinic Phase 2 = Tetragonal
Space group	Phase 1 = $I2/c$ Phase 2 = $I4_1/a$	Phase 1 = $I2/c$ Phase 2 = $I4_1/a$	Phase 1 = $I2/c$ Phase 2 = $I4_1/a$
Lattice parameters	Phase 1: a = 5.4227 (1) Å b = 11.6195 (3) Å c = 5.3681 (1) Å β = 90.521 (1)° Phase 2: a = 5.3928 (1) Å c = 11.6201 (2) Å	Phase 1: a = 5.4473 (1) Å b = 11.5995 (3) Å c = 5.3303 (1) Å β = 91.116 (2)° Phase 2: a = 5.3911 (1) Å c = 11.6148 (2) Å	Phase 1: a = 5.4711 (2) Å b = 11.6076 (4) Å c = 5.31187 (2) Å β = 91.564 (2)° Phase 2: a = 5.3926 (2) Å c = 11.6191 (4) Å
Volume	Phase 1 = 338.22 (1) Å^3 Phase 2 = 337.94 (2) Å^3	Phase 1 = 336.74 (1) Å^3 Phase 2 = 337.56 (1) Å^3	Phase 1 = 337.21 (2) Å^3 Phase 2 = 337.89 (2) Å^3
Density (calc)	Phase 1 = 5.979 Mg m^{-3} Phase 2 = 5.984 Mg m^{-3}	Phase 1 = 6.005 Mg m^{-3} Phase 2 = 5.988 Mg m^{-3}	Phase 1 = 6.003 Mg m^{-3} Phase 2 = 5.973 Mg m^{-3}
Weight fraction	Phase 1 = 0. 760 (8) Phase 2 = 0.240 (5)	Phase 1 = 0.840 (2) Phase 2 = 0.160 (3)	Phase 1 = 0.85 (12) Phase 2 = 0.14 (7)
R-factors	R_{wp} = 14.7 R_p = 21.8 R_{ex} = 8.70	R_{wp} = 16.7 R_p = 21.5 R_{ex} = 8.91	R_{wp} = 16.4 R_p = 20.7 R_{ex} = 8.97

Table S3. Crystal and refinement parameters calculated for $LaNb_{0.7}Sb_{0.3}O_{4-\delta}$ at -150°C calculated on the basis of X-Ray diffractograms. Estimated standard deviations are given in parentheses.

Temperature	-150°C
Crystal system	Phase 1 = Monoclinic Phase 2 = Tetragonal
Space group	Phase 1 = $I2/c$ Phase 2 = $I4_1/a$
Lattice parameters	Phase 1: a = 5.4827 (1) Å b = 11.5872 (2) Å c = 5.2969 (1) Å β = 91.870 (1)° Phase 2: a = 5.3902 (3) Å c = 11.5949 (3) Å
Volume	Phase 1 = 336.33 (1) $Å^3$ Phase 2 = 336.88 (3) $Å^3$
Density (calc)	Phase 1 = 6.013 Mg m^{-3} Phase 2 = 6.004 Mg m^{-3}
Weight fraction	Phase 1 = 0.896 (8) Phase 2 = 0.103 (1)
R-factors	R_{wp} = 17.4 R_p = 21.7 R_{ex} = 8.80

Table S4. Refined atomic coordinates, thermal parameters, and significant contact distances for $LaNb_{0.9}Sb_{0.1}O_{4-\delta}$ at 20 °C. Estimated standard deviations are given in parentheses.

(a) Atomic parameters

Atom	site	x	y	z	Occ.	U_{eqv} ($Å^2$)
La	4*e*	0.00	0.62900(5)	0.25	1.0	0.0050(4)
Nb/Sb	4*e*	0.00	0.10639(5)	0.25	0.9/0.1	0.0049(4)
O1	8*f*	0.23897(8)	0.03370(4)	0.05867(9)	1.0	0.0099(4)
O2	8*f*	0.14976(10)	0.20529(4)	0.48992(9)	0.992(2)	0.0086(4)

(b) Anisotropic thermal parameters

Atom	U_{11} (Å^2)	U_{22} (Å^2)	U_{33} (Å^2)	U_{12} (Å^2)	U_{13} (Å^2)	U_{23} (Å^2)
La	0.0045(2)	0.0042(2)	0.0062(2)	0.0	0.0008(1)	0.0
Nb/Sb	0.0051(2)	0.0071(3)	0.0025(2)	0.0	0.0016(2)	0.0
O1	0.0093(2)	0.0090(2)	0.0114(2)	0.0029(2)	0.0041(2)	0.0026(2)
O2	0.0081(2)	0.0085(2)	0.0094(2)	0.0014(2)	-0.0025(2)	-0.0015(2)

(c) Significant contact distances (Å)

La-O1	2.4903(5) × 2		Nb/Sb-O1	1.9049(5) × 2
La-O1′	2.5403(6) × 2		Nb/Sb-O2	1.8543(6) × 2
La-O2	2.5187(6) × 2			
La-O2′	2.4649(6) × 2			

Table S5. Refined atomic coordinates, thermal parameters and significant contact distances for $LaNb_{0.75}Sb_{0.25}O_{4-\delta}$ at 20 °C. Estimated standard deviations are given in parentheses

(a) Phase 1 Atomic parameters

Atom	site	x	y	z	Occ.	U_{eqv} (Å²)
La	4*e*	0.00	0.62730(8)	0.25	1.0	0.0044(5)
Nb/Sb	4*e*	0.00	0.11588(10)	0.25	0.75/0.25	0.0062(8)
O1	8*f*	0.2433(1)	0.03607(8)	0.0759(2)	1.0	0.0107(7)
O2	8*f*	0.1529(2)	0.20760(7)	0.4932(1)	1.0	0.0078(6)

(b) Phase 1 Anisotropic thermal parameters

Atom	U_{11} (Å²)	U_{22} (Å²)	U_{33} (Å²)	U_{12} (Å²)	U_{13} (Å²)	U_{23} (Å²)
La	0.0048(3)	0.0053(3)	0.0030(3)	0.0	-0.0001(1)	0.0
Nb/Sb	0.0038(4)	0.0085(5)	0.0052(5)	0.0	0.0012(3)	0.0
O1	0.0112(4)	0.0099(4)	0.0110(4)	0.0043(3)	0.0053(3)	0.0041(3)
O2	0.0071(3)	0.0079(3)	0.0084(3)	0.0028(3)	-0.0011(3)	0.0005(3)

(c) Phase 1 Significant contact distances (Å)

La-O1	2.4973(9) × 2		Nb/Sb-O1	1.8877(10) × 2
La-O1′	2.5210(11) × 2		Nb/Sb-O2	1.8541(11) × 2
La-O2	2.5114(10) × 2			
La-O2′	2.4876(9) × 2			

(d) Phase 2 Atomic parameters

Atom	site	x	y	z	Occ.	U_{iso} (Å²)
La	4*b*	0.00	0.25	0.625	1.0	0.0081(11)
Nb/Sb	4*a*	0.00	0.25	0.125	0.75/0.25	0.034(3)
O1	16*f*	0.2431(13)	0.0885(13)	0.0374(7)	1.0	0.036(2)

(e) Phase 2 Significant contact distances (Å)

La-O1	2.507(7) × 4		Nb/Sb-O1	1.874(7) × 4

La-O1′	2.497(8) × 4			

Table S6. Refined atomic coordinates, thermal parameters and significant contact distances for $LaNb_{0.7}Sb_{0.3}O_{4-\delta}$ at 20 °C. Estimated standard deviations are given in parentheses

(a) Atomic parameters

Atom	site	x	y	z	Occ.	U_{eqv} (Å^2)
La	4*b*	0.00	0.25	0.625	1.0	0.0055(4)
Nb/Sb	4*a*	0.00	0.25	0.125	0.7/0.3	0.0074(6)
O1	16*f*	0.2438(1)	0.0881(1)	0.03932(5)	1.0	0.0111(4)

(b) Anisotropic thermal parameters

Atom	U_{11} (Å^2)	U_{22} (Å^2)	U_{33} (Å^2)	U_{12} (Å^2)	U_{13} (Å^2)	U_{23} (Å^2)
La	0.0055(2)	0.0055(2)	0.0055(3)	0.0	0.0	0.0
Nb/Sb	0.0051(3)	0.0051(3)	0.0121(4)	0.0	0.0	0.0
O1	0.0112(3)	0.0132(3)	0.0089(2)	0.0066(3)	0.0041(2)	0.0032(2)

(c) Significant contact distances (Å)

La-O1	2.4980(6) × 4		Nb/Sb-O1	1.8684(6) × 4
La-O1′	2.5168(6) × 4			

(a)

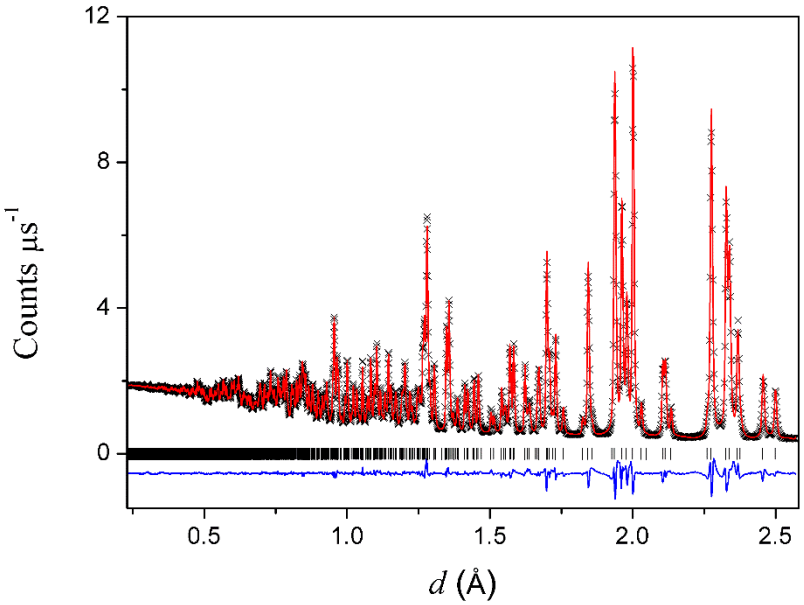

(b)

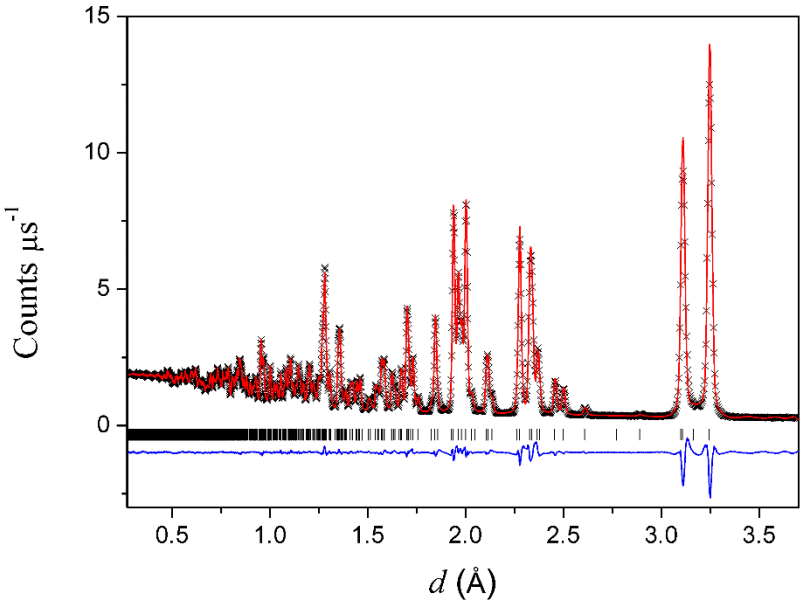

Figure S2. Fitted neutron diffraction profiles for $LaNb_{0.9}Sb_{0.1}O_{4-\delta}$ showing data from (a) neutron back scattering and (b) 90° detector banks. Observed (+ symbols),

calculated (line) and difference (lower) profiles are shown with reflection positions indicated by markers.

(a)

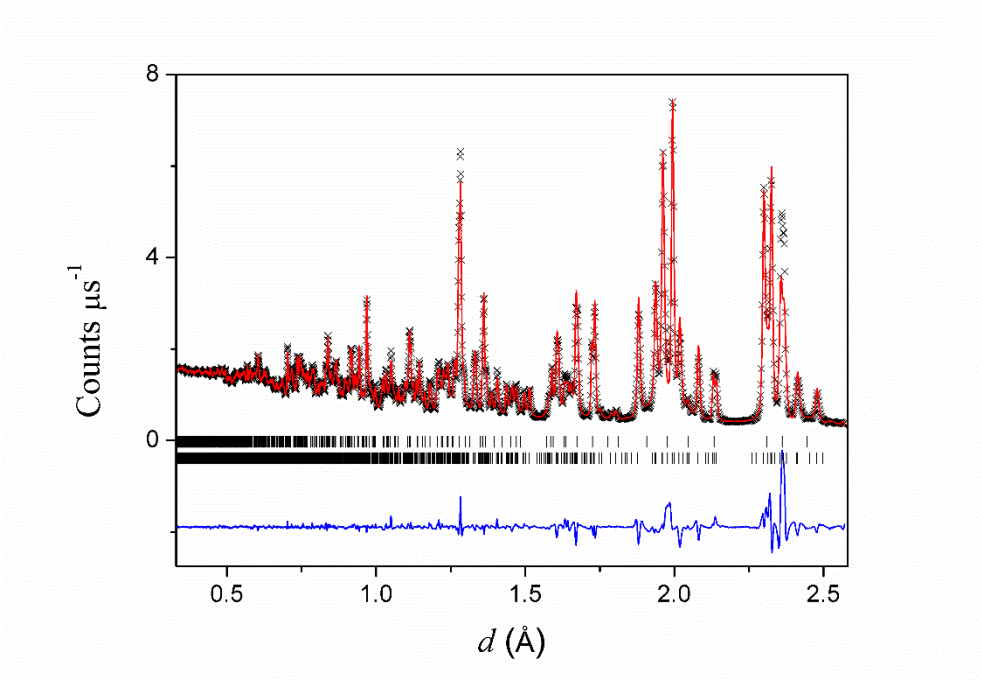

(b)

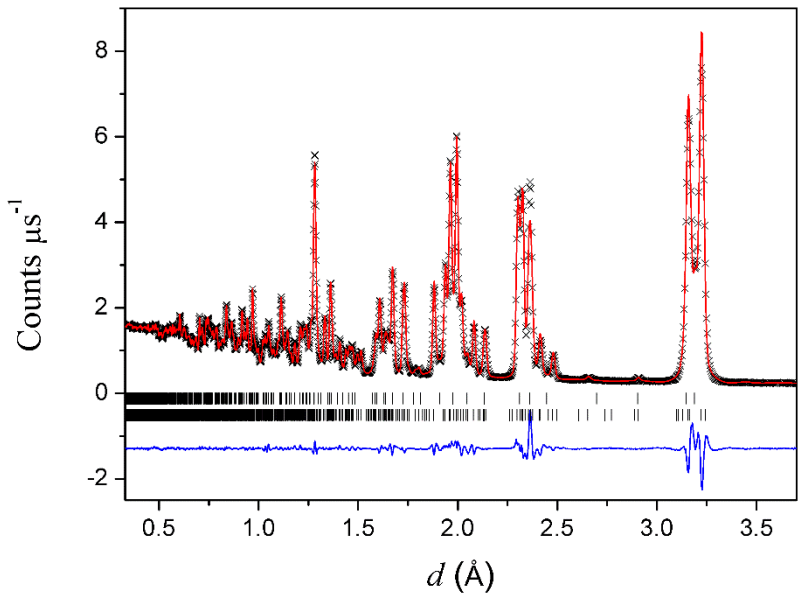

Figure S3. Fitted neutron diffraction profiles for $LaNb_{0.75}Sb_{0.25}O_{4-\delta}$ showing data from (a) neutron back scattering and (b) 90° detector banks. Observed (+ symbols), calculated (line) and difference (lower) profiles are shown with reflection positions indicated by markers (lower: phase 1 and upper: phase 2).

(a)

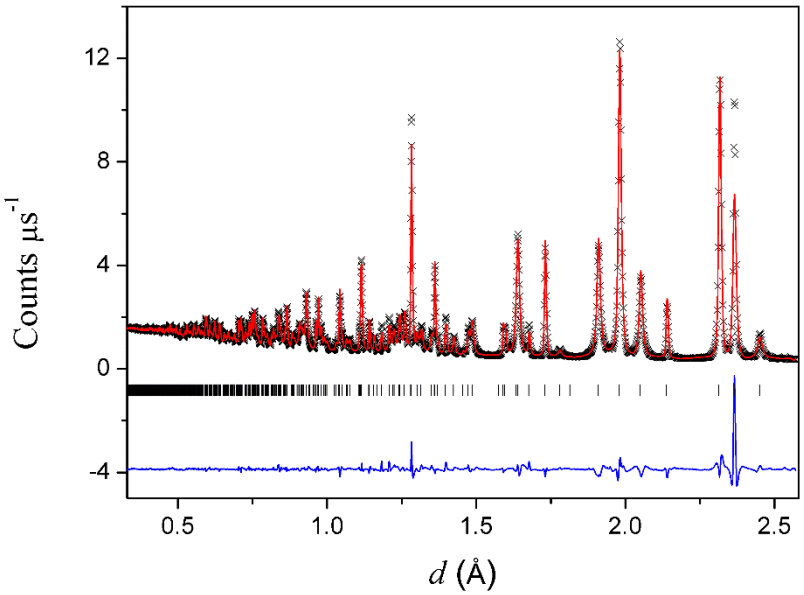

(b)

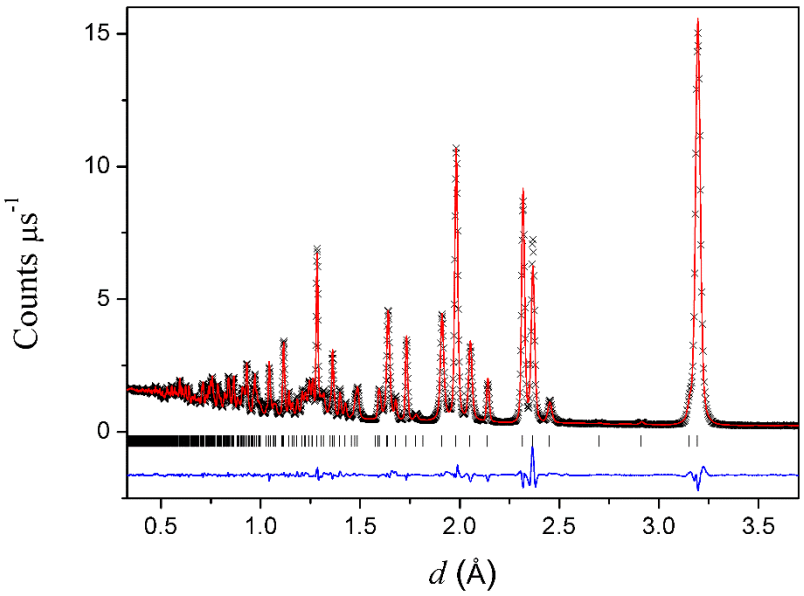

Figure S4. Fitted neutron diffraction profiles for $LaNb_{0.7}Sb_{0.3}O_{4-\delta}$ showing data from (a) neutron back scattering and (b) 90° detector banks. Observed (+ symbols),

calculated (line) and difference (lower) profiles are shown with reflection positions indicated by markers.

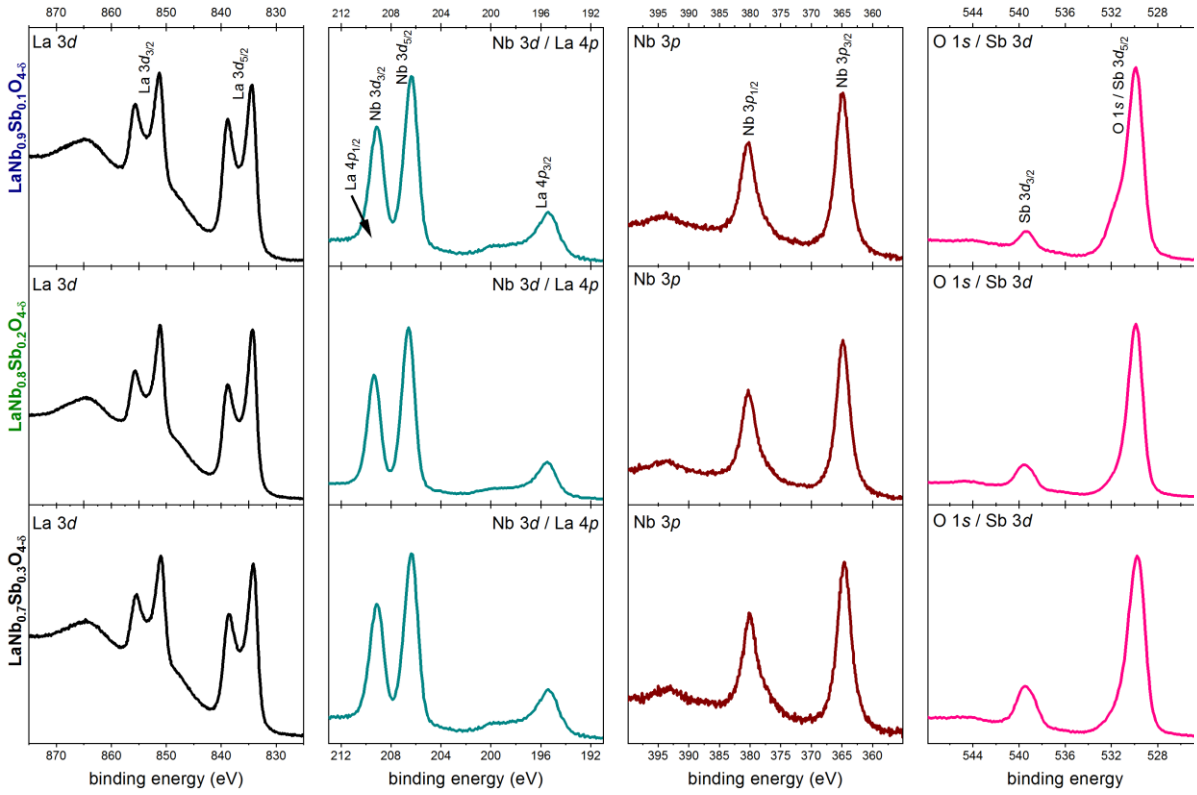

Figure S5. Nb 3*d* core level X-ray photoelectron spectra for $LaNb_{1-x}Sb_xO_{4-\delta}$ ceramics

(a)

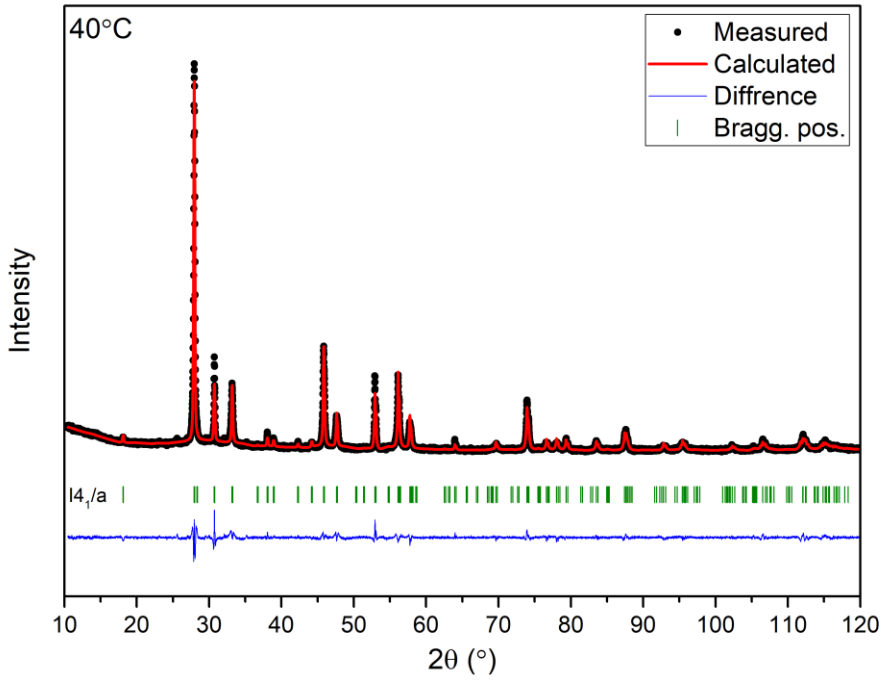
40°C
Measured
Calculated
Diffrence
Bragg. pos.
Intensity
I4$_1$/a
10 20 30 40 50 60 70 80 90 100 110 120
2θ (°)

(b)

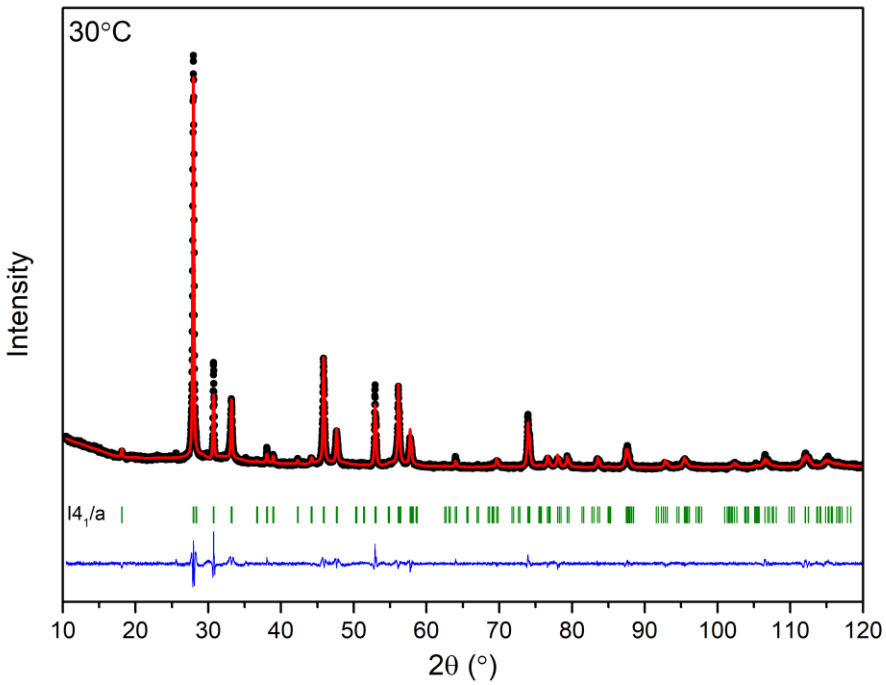
30°C
Intensity
I4$_1$/a
10 20 30 40 50 60 70 80 90 100 110 120
2θ (°)

(c)

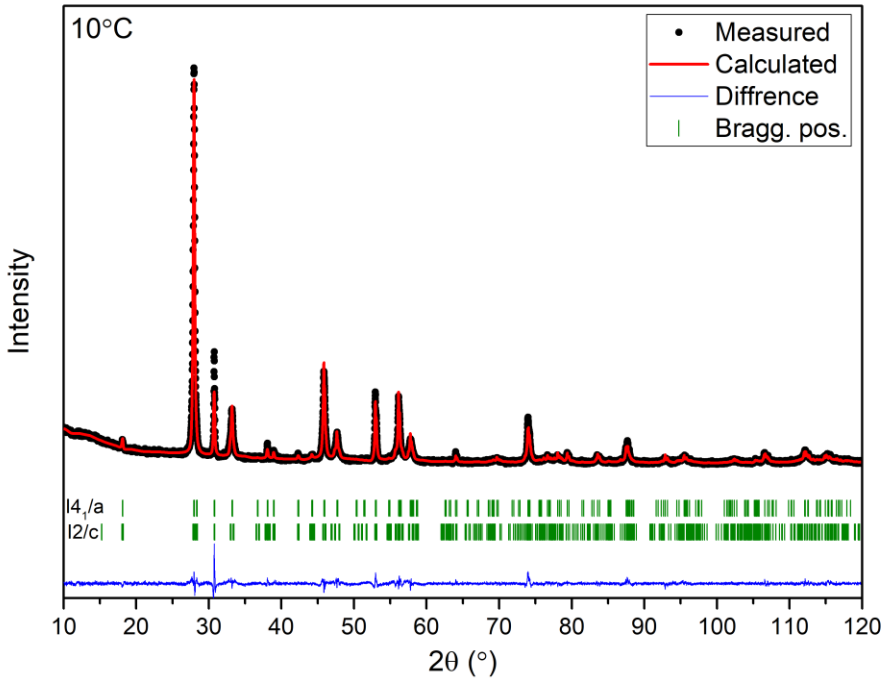
10°C
Measured
Calculated
Diffrence
Bragg. pos.
Intensity
I4₁/a
I2/c
10 20 30 40 50 60 70 80 90 100 110 120
2θ (°)

(d)

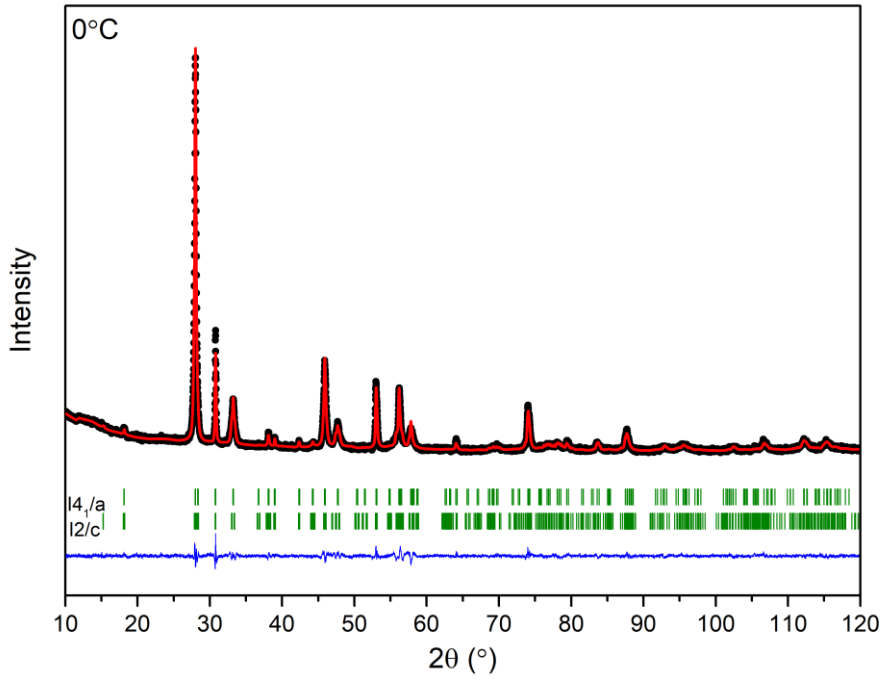
0°C
Intensity
I4₁/a
I2/c
10 20 30 40 50 60 70 80 90 100 110 120
2θ (°)

(e)

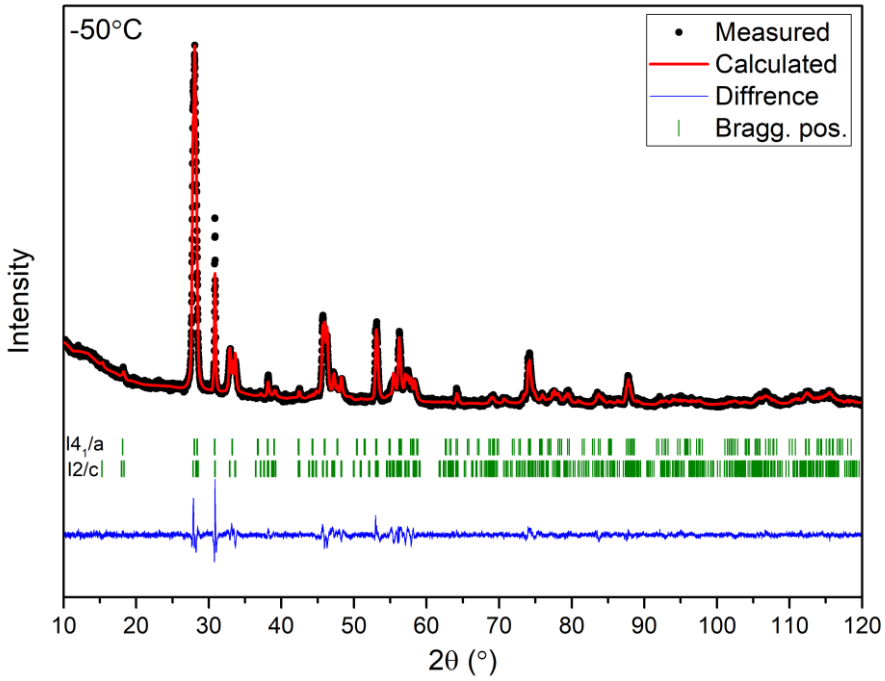
-50°C
Measured
Calculated
Diffrence
Bragg. pos.
Intensity
I4$_1$/a
I2/c
10 20 30 40 50 60 70 80 90 100 110 120
2θ (°)

(f)

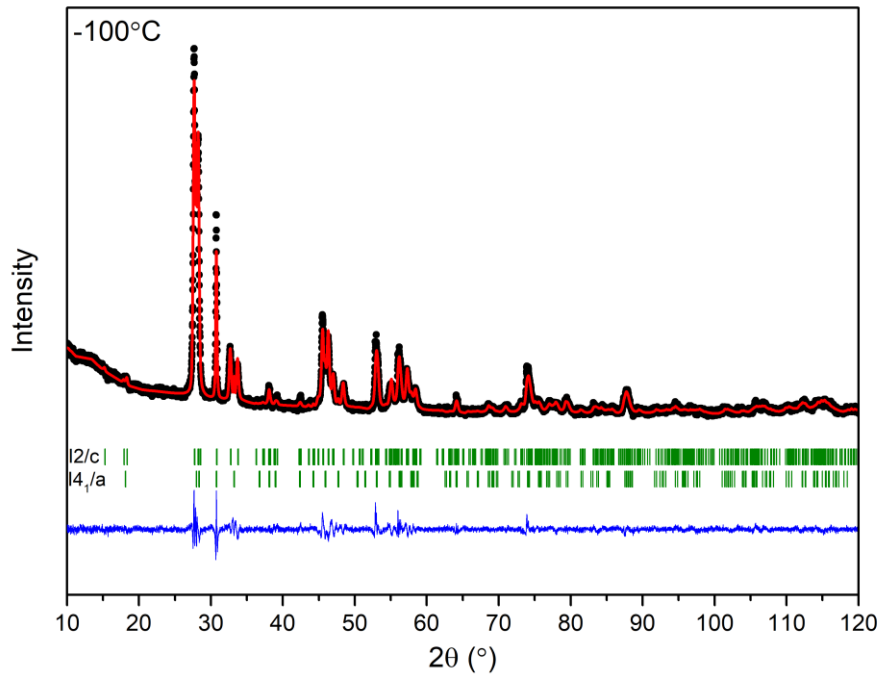
-100°C
Intensity
I2/c
I4$_1$/a
10 20 30 40 50 60 70 80 90 100 110 120
2θ (°)

(g)

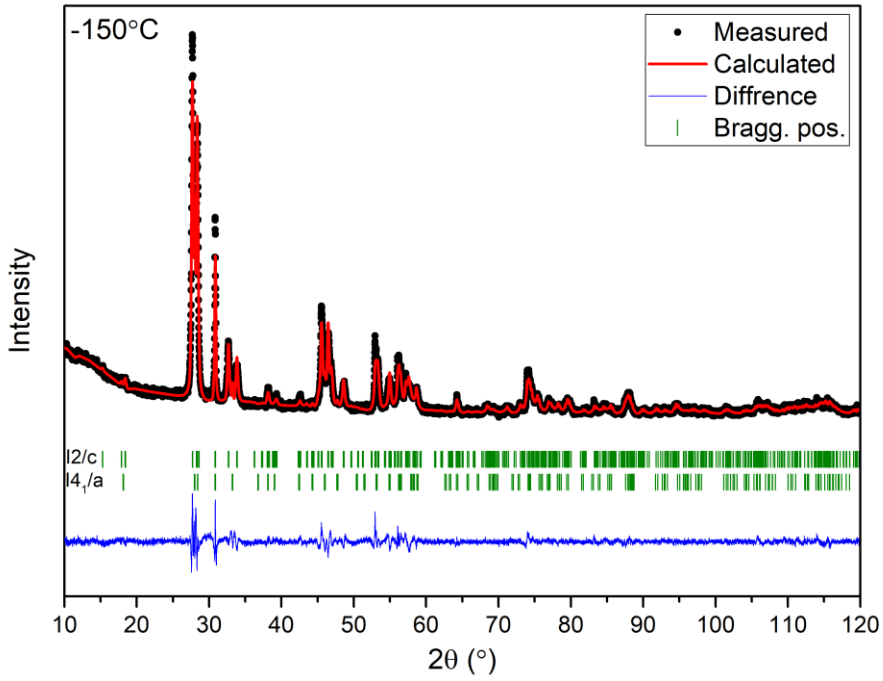

Figure S5. Fitted X-Ray diffraction profiles for $LaNb_{0.7}Sb_{0.3}O_{4-\delta}$ showing data for temperatures (a) 40°C, (b) 30°C, (c) 10°C, (d) 0°C, (e) -50°C, (f) -100°C and (g) -150°C . Observed (• symbols), calculated (line) and difference (lower) profiles are shown with reflection positions indicated by markers.

Table S4. Crystal and refinement parameters calculated for $LaNb_{0.7}Sb_{0.3}O_{4-\delta}$ at 40°C, 30°C and 10°C calculated on the basis of X-Ray diffractograms. Estimated standard deviations are given in parentheses.

Temperature	40°C	30°C	10°C
Crystal system	Monoclinic	Monoclinic	Phase 1 = Monoclinic Phase 2 = Tetragonal
Space group	$I2/c$	$I2/c$	Phase 1 = $I2/c$ Phase 2 = $I4_1/a$
Lattice parameters	a = 5.3961 (1) Å c = 11.6339 (2) Å	a = 5.3960 (1) Å c = 11.6331 (2) Å	Phase 1: a = 5.4272 (1) Å b = 11.6234 (3) Å c = 5.3652 (1) Å β = 91.710(1)° Phase 2: a = 5.3939 (1) Å c = 11.6266 (2) Å
Volume	338.75 (2) Å^3	338.72 (3) Å^3	Phase 1 = 338.43 (4) Å^3 Phase 2 = 338.28 (2) Å^3
Density (calc)	5.970 Mg m^{-3}	5.970 Mg m^{-3}	Phase 1 = 5.978 Mg m^{-3} Phase 2 = 5.978 Mg m^{-3}
Weight fraction	100	100	Phase 1 = 0.393(9) Phase 2 = 0.607(7)
R-factors	R_{wp} = 17.8 R_p = 24.8 R_{ex} = 8.53	R_{wp} = 18.3 R_p = 25.8 R_{ex} = 8.71	R_{wp} = 16.6 R_p = 24.2 R_{ex} = 3.61

Table S5. Crystal and refinement parameters calculated for $LaNb_{0.7}Sb_{0.3}O_{4-\delta}$ at 0°C, -50°C and -100°C calculated on the basis of X-Ray diffractograms. Estimated standard deviations are given in parentheses.

Temperature	0°C	-50°C	-100°C
Crystal system	Phase 1 = Monoclinic Phase 2 = Tetragonal	Phase 1 = Monoclinic Phase 2 = Tetragonal	Phase 1 = Monoclinic Phase 2 = Tetragonal
Space group	Phase 1 = $I2/c$ Phase 2 = $I4_1/a$	Phase 1 = $I2/c$ Phase 2 = $I4_1/a$	Phase 1 = $I2/c$ Phase 2 = $I4_1/a$
Lattice parameters	Phase 1: a = 5.4227 (1) Å b = 11.6195 (3) Å c = 5.3681 (1) Å β = 90.521 (1)° Phase 2: a = 5.3928 (1) Å c = 11.6201 (2) Å	Phase 1: a = 5.4473 (1) Å b = 11.5995 (3) Å c = 5.3303 (1) Å β = 91.116 (2)° Phase 2: a = 5.3911 (1) Å c = 11.6148 (2) Å	Phase 1: a = 5.4711 (2) Å b = 11.6076 (4) Å c = 5.31187 (2) Å β = 91.564 (2)° Phase 2: a = 5.3926 (2) Å c = 11.6191 (4) Å
Volume	Phase 1 = 338.22 (1) Å^3 Phase 2 = 337.94 (2) Å^3	Phase 1 = 336.74 (1) Å^3 Phase 2 = 337.56 (1) Å^3	Phase 1 = 337.21 (2) Å^3 Phase 2 = 337.89 (2) Å^3
Density (calc)	Phase 1 = 5.979 Mg m^{-3} Phase 2 = 5.984 Mg m^{-3}	Phase 1 = 6.005 Mg m^{-3} Phase 2 = 5.988 Mg m^{-3}	Phase 1 = 6.003 Mg m^{-3} Phase 2 = 5.973 Mg m^{-3}
Weight fraction	Phase 1 = 0. 760 (8) Phase 2 = 0.240 (5)	Phase 1 = 0.840 (2) Phase 2 = 0.160 (3)	Phase 1 = 0.85 (12) Phase 2 = 0.14 (7)
R-factors	R_{wp} = 14.7 R_p = 21.8 R_{ex} = 8.70	R_{wp} = 16.7 R_p = 21.5 R_{ex} = 8.91	R_{wp} = 16.4 R_p = 20.7 R_{ex} = 8.97

Table S6. Crystal and refinement parameters calculated for $LaNb_{0.7}Sb_{0.3}O_{4-\delta}$ at -150°C calculated on the basis of X-Ray diffractograms. Estimated standard deviations are given in parentheses.

Temperature	-150°C
Crystal system	Phase 1 = Monoclinic Phase 2 = Tetragonal
Space group	Phase 1 = $I2/c$ Phase 2 = $I4_1/a$
Lattice parameters	Phase 1: a = 5.4827 (1) Å b = 11.5872 (2) Å c = 5.2969 (1) Å β = 91.870 (1)° Phase 2: a = 5.3902 (3) Å c = 11.5949 (3) Å
Volume	Phase 1 = 336.33 (1) $Å^3$ Phase 2 = 336.88 (3) $Å^3$
Density (calc)	Phase 1 = 6.013 Mg m^{-3} Phase 2 = 6.004 Mg m^{-3}
Weight fraction	Phase 1 = 0.896 (8) Phase 2 = 0.103 (1)
R-factors	R_{wp} = 17.4 R_p = 21.7 R_{ex} = 8.80